

Compressive Confocal Microscopy: 3D Reconstruction Algorithms

P. Ye, J. L. Paredes^a, Y. Wu, C. Chen, G. R. Arce and D. W. Prather

Department of Electrical and Computer Engineering,
University of Delaware, Newark, DE, 19716 USA

^a Department of Electrical Engineering,
University of Los Andes, Mérida, 5101 Venezuela

ABSTRACT

In this paper, a new approach for Confocal Microscopy (CM) based on the framework of compressive sensing is developed. In the proposed approach, a point illumination and a random set of pinholes are used to eliminate out-of-focus information at the detector. Furthermore, a Digital Micromirror Device (DMD) is used to efficiently scan the 2D or 3D specimen but, unlike the conventional CM that uses CCD detectors, the measured data in the proposed compressive confocal microscopy (CCM) emerge from random sets of pinhole illuminated pixels in the specimen that are linearly combined (projected) and measured by a single photon detector. Compared to conventional CM or programmable array microscopy (PAM), the number of measurements needed for nearly perfect reconstruction in CCM is significantly reduced. Our experimental results are based on a testbed that uses a Texas Instruments DMD (an array of 1024×768 ; $13.68 \times 13.68 \mu\text{m}^2$ mirrors) for computing the linear projections of illuminated pixels and a single photon detector is used to obtain the compressive sensing measurement. The position of each element in the DMD is defined by the compressed sensing measurement matrices. Three-dimensional image reconstruction algorithms are developed that exploit the inter-slice spatial image correlation as well as the correlation between different 2D slices. A comprehensive performance comparison between several binary projection patterns is shown. Experimental and simulation results are provided to illustrate the features of the proposed systems.

Keywords: confocal imaging, compressive sensing, programmable array microscopy, SBHE, DMD

1. INTRODUCTION

Confocal microscopy is an imaging technique of increasing interest in several fields of science and medicine.¹ It has been widely used in the study of cell and tissue in biology, genetics, microbiology and in surface inspections in the semiconductor industry, among other applications. Compared to conventional wide-field microscopy, confocal microscopy offers improved performance in contrast and information capacity of the underlying image by rejecting out-of-focus background. Furthermore, this technique has the ability to capture thin optical sections from thick specimens and the ability to have controllable depth of field. However, conventional confocal microscopy has the shortcoming of demanding time-consuming scanning over 2D or 3D raster patterns, since image points are illuminated and detected one at a time.

In order to speed-up the image acquisition time while still preserving the desirable optical sectioning characteristic, parallel confocal microscopy has been developed. The first parallel confocal imaging system is known as the tandem scanning microscope,² where a Nipkov disc is used for illuminating and detecting multiple object's points at the same time. This approach, however, suffers from low light efficiency. To overcome this limitation Liang et al.³ developed a programmable multiple-aperture confocal imaging system based on a DMD instead of the Nipkov disk improving both light-utilization efficiency and confocal image rate. Architectures based on

Further author information:

Gonzalo R. Arce: E-mail: arce@ee.udel.edu

Peng Ye: E-mail: pengye@udel.edu

This research was supported in part by the National Science Foundation through the grant EECS-0725422 and by the Office of Naval Research under the grant N00014-07-1-0393.

programmable array microscopes (PAM)⁴ are of great interest as these are based on coded illumination patterns readily attained by DMD, which combines the DMD with the aperture-correlation technique.⁵ All these parallel confocal imaging systems follow the rule of conventional imaging system, in which a large amount of data is firstly acquired at the Nyquist rate and then compressed exploiting the 2D and 3D redundancy presented in the acquired images. An obvious drawback of these systems is that in the compression procedure a great percentage of raw data is discarded. While reducing the scanning time due to the parallel nature of PAM systems, these approaches are still limited by Nyquist sampling rates. With the advent of compressive sensing (CS) theory,^{6,7} compressive imaging systems which combine sampling and compression into a single non-adaptive linear measurement process have become possible to reduce the acquisition time and simplify the imaging acquisition system.

In this paper, we propose a new confocal imaging system called compressive confocal microscopy (CCM). Unlike conventional CM, in the proposed CCM, a DMD is used to perform the optical computation of linear projections of multiple points in focal image plane. Each projection is obtained for a particular position of the micromirrors in DMD defined by a measurement matrix. The design of the projection matrices is based on the rich theory of compressive sensing, which is a new framework for simultaneous sampling and compressing signals. The proposed system offers high image acquisition speed, sub-Nyquist sampling rate and effective optical sectioning. Furthermore, it has the advantage of simplifying the hardware and optical complexity, by using a single detector instead of CCD sensor array and by off-loading the processing from the data acquisition into the image reconstruction which is performed digitally in a standard computer.

The rest of the paper is organized as follows. In Section 2, we give a general introduction to CCM, which has been presented in our earlier work.⁸ In Section 3, we introduce new 3D joint image reconstruction algorithms based on CS theory. Then, we conduct a theoretical analysis of CCM in Section 4. Finally, in Section 5, we draw our conclusions.

2. COMPRESSIVE CONFOCAL MICROSCOPY

2.1 Preliminary Background

Given a signal $X \in \mathcal{R}^N$ and some dictionary of basis functions $\Psi = [\psi_1, \psi_2, \dots, \psi_Z]$ with $\psi_i \in \mathcal{R}^N$, we say that X is T -sparse or compressible in Ψ if it can be approximated by a linear combination of T vectors from Ψ with $T \ll N$, i.e. $X \approx \sum_{i=1}^T \theta_{\ell_i} \psi_{\ell_i} = \Psi\Theta$. The dictionary Ψ is a collection of parameterized waveforms, called atoms, and may contain Fourier basis, Wavelet basis, cosine packets, Chirplets basis, or even a combination of orthogonal basis and tight-frame. For instance, natural images tend to be sparse in the discrete cosine transform (DCT) and wavelet bases, hence, those bases can be suitably used to define a dictionary for image representation. The theory of CS shows that, with high probability, a signal X can be recovered from a reduced set of random projections. More precisely, given $Y = \Phi X$, where Φ is an $K \times N$ random measurement matrix with its rows incoherent with the columns of Ψ . The original signal X can be recovered from the set of random projections Y by solving the following optimization problem:⁹

$$\operatorname{argmin}_{X \in \mathcal{R}^N} \|\Phi X - Y\|_2^2 + \lambda \|\Theta\|_1 \quad (1)$$

where $\lambda > 0$ is the regularization parameter. The number of measurements needed to keep the relevant information about the original signal has to be equal to $CT \log N \ll N$, where $C \geq 1$ is an oversampling factor. Commonly used random measurement matrices Φ for CS are random Gaussian matrices ($\phi_{ij} \sim \mathcal{N}(0, 1/N)$), Bernoulli matrices ($\phi_{ij} \in \{\pm 1\}$) and randomly permuted vector from standard orthogonal bases such as Fourier, Walsh-Hadamard or Noiselet bases. In the application at hand, the measurement matrices must be designed such that they fit our hardware profile, i.e. they can be implemented in a DMD. Thus, Walsh-Hadamard bases having binary values are well suited for our application. In this work, we propose to use two Walsh-Hadamard transform based measurement systems: Ordered Hadamard ensemble (ODHE) and Scrambled Block Hadamard ensemble (SBHE)¹⁰ to define a set of measurement binary matrices that are used to generate DMD modulation patterns. The measured data in the proposed CCM emerge from random sets of pinhole illuminated pixels in the specimen that are linearly combined and measured by a single photon detector. The optical calculations of linear projections of an image is performed by a Texas Instruments DMD. That is, a DMD is placed at the

primary image plane of the objective to introduce the illumination patterns as well as the detector masks. The core part of the DMD is an XGA (768(V) × 1024(H)) format array of aluminum micro-mirrors with a pitch of 13.68 μm. Each mirror can be individually deflected at an angle of ±12° about the hinged diagonal axis. The deflection condition of each mirror is controlled by a CMOS addressing circuit. Thus, each mirror can either be deflected at an angle of +12° ('on' condition) or −12° ('off' condition). The ±12° position of each micromirror corresponds to a particular entry of the measurement binary matrix. The modulation pattern of the DMD produces a structured illumination on the specimen. The emission (or reflection) light from the specimen is then imaged back onto the DMD and from there, via a beam splitter and relay optics, onto a single photon detector. The contributions from all micromirrors at the 'on' position define a conjugate measurement, which is a random projection of the in-focus plane. Successively, changing the location of the 'on' mirrors according to a random pattern (measurement matrix) leads to a sequence of compressive measurements which can then be used to reconstruct the in-focus plane.

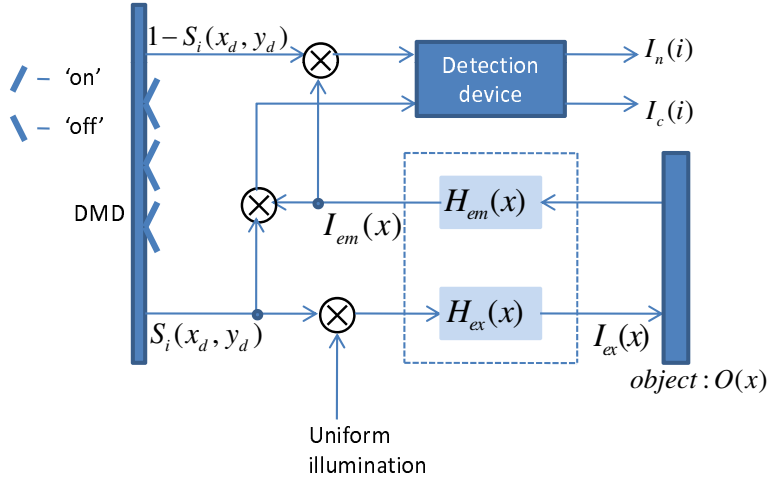


Figure 1. System diagram of the compressive confocal microscope.

Figure 1 shows the “flow of data” in the proposed CCM. Following the approach in Ref[4], the i -th modulation pattern of a DMD is given by

$$S_i(x_d, y_d) = \begin{cases} 1 & \text{if } (x_d, y_d) \text{ is on a mirror that is 'on'} \\ 0 & \text{if } (x_d, y_d) \text{ is on a mirror that is 'off'} \end{cases} \quad (2)$$

where (x_d, y_d) is the two-dimensional (2D) coordinate system on the DMD plane, with $(0, 0)$ as the center of DMD. It can be shown that the illumination pattern of a given object is given by

$$I_{ex}(x_o, y_o, z_o; i) = \iint_{-\infty}^{+\infty} S_i(Mu, Mv) \times H_{ex}(x_o - u, y_o - v, z_o) dudv, \quad (3)$$

where M and H_{ex} are, respectively, the magnification and the excitation point spread function (PSF) of the objective. (x_o, y_o, z_o) denotes a three-dimensional (3D) coordinate system for the object $O(x_o, y_o, z_o)$, where $x_o = \frac{x_d}{M}$, $y_o = \frac{y_d}{M}$ and z_o defines the axial position of the illuminated plane.

The i -th conjugate measurement is formed by adding up the contributions of reflected light off mirror elements at the 'on' position over the entire $L \times W$ DMD array. This is,

$$I_c(i) = \int_{-\frac{L \times \rho}{2}}^{\frac{L \times \rho}{2}} \int_{-\frac{W \times \rho}{2}}^{\frac{W \times \rho}{2}} \iiint_{-\infty}^{+\infty} H_{em}\left(\frac{x_d}{M} - u, \frac{y_d}{M} - v, w\right) I_{ex}(u, v, w; i) O(u, v, w - z_s) dudvdw S_i(x_d, y_d) dx_d dy_d, \quad (4)$$

where ρ is the size of DMD micromirror and H_{em} is the emission PSF of the objective. Likewise, the contributions

from the mirror elements at the 'off' position define the non-conjugate measurement, namely

$$I_n(i) = \int_{-\frac{L \times \rho}{2}}^{\frac{L \times \rho}{2}} \int_{-\frac{W \times \rho}{2}}^{\frac{W \times \rho}{2}} \iiint_{-\infty}^{+\infty} H_{em} \left(\frac{x_d}{M} - u, \frac{y_d}{M} - v, w \right) \times I_{ex}(u, v, w; i) O(u, v, w - z_s) dudvdw (1 - S_i(x_d, y_d)) dx_d dy_d, \quad (5)$$

The modulation pattern S_i has to be defined in some optimal fashion, since it incorporates the randomness needed to project the image of interest into a random basis. To illustrate this point better, consider a 2D image F of size $N \times N$, where $F = \{f(m, n)\}, n = 1, 2, \dots, N; m = 1, 2, \dots, N$. Furthermore, suppose F is sparse or compressible on some fixed basis. Let Φ be a $N \times N$ random binary sensing matrix. Projecting F onto Φ yields: $Y = \Phi F \Phi^H$, where H denotes the transpose conjugate operator and $Y = \{y(m, n)\}, m = 1, 2, \dots, N; n = 1, 2, \dots, N$ is the compressive measurement. It can be shown that the projection operation reduces to:

$$y(m, n) = \langle B^{m,n}, F \rangle, \quad (6)$$

where the set $\{B^{m,n}\}$ is referred to as a measurement ensemble where each $\{B^{m,n}\}$ is a $N \times N$ binary matrix, $B^{m,n} \in [-1, 1]^{(N \times N)}$. Two different sensing systems that have been found to speed up the signal reconstruction process are used to define the modulation pattern $\{B^{m,n}\}$. They are Ordered Hadamard Ensemble (ODHE) and Scrambled Block Hadamard Ensemble (SBHE).¹⁰ For the former, the measurement ensemble to be loaded onto DMD is defined as:

$$B^{m,n} = H Z^{m,n} H^T \quad (7)$$

where H is the Hadamard transform matrix and $Z^{m,n}$ is an $N \times N$ matrix with just a non-zero entry at position (m, n) . The non-zero entry in $Z^{m,n}$ is set to 1. Thus, by randomly selecting the (m, n) position where the non-zero value is placed, a set of measurement matrices is defined.

For SBHE, the modulation pattern is defined according to:

$$B^{m,n} = P_{N^2}^{-1} W^{-1} Z^{m,n} \quad (8)$$

where $Z^{m,n}$ is a matrix with just one non-zero entry at the (m, n) position, P_{N^2} represents N^2 points scramble operator and W is a block Hadamard transform operator of block size BS.¹⁰

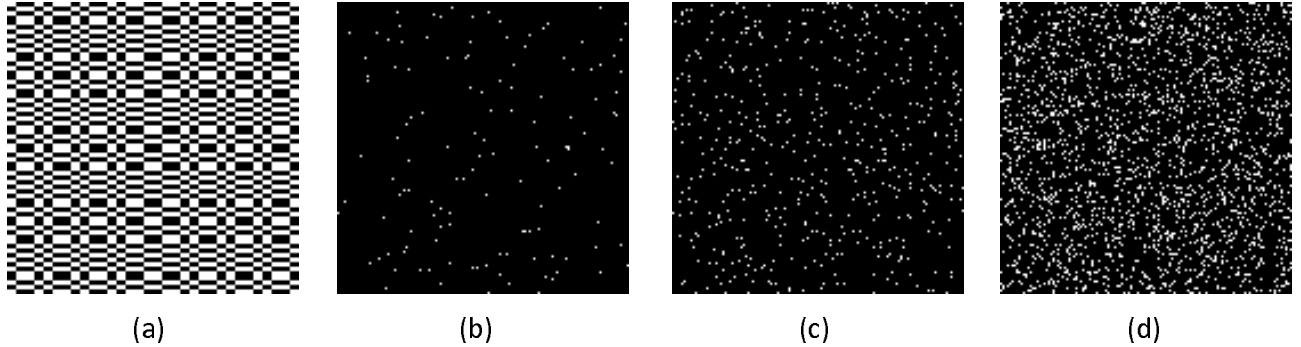


Figure 2. Example of modulation patterns, image size 128×128 . (a) ODHE pattern, percentage of openings 50%. (b) SBHE pattern, BS=16, percentage of openings 0.78%. (c) SBHE pattern, BS=32, percentage of openings 3.13%. (d) SBHE pattern, BS=64, percentage of openings 12.50%.

Figure 2 depicts illustrative examples of an ODHE and a SBHE modulation patterns, where percentage of openings represents the percentage of 'on' mirrors in the entire mirror array and BS stands for block size. In block Hadamard transform,¹¹ the underlying image is divided into $BS \times BS$ image blocks and a Hadamard transform is performed on each small block. As can be seen, the SBHE pattern is much sparser than the ODHE pattern. In turn, the light efficiency becomes much lower. Figure 3 shows the normalized axial response of an infinitely thin plane with different modulation patterns. As can be seen from Fig. 3, the SBHE pattern offers

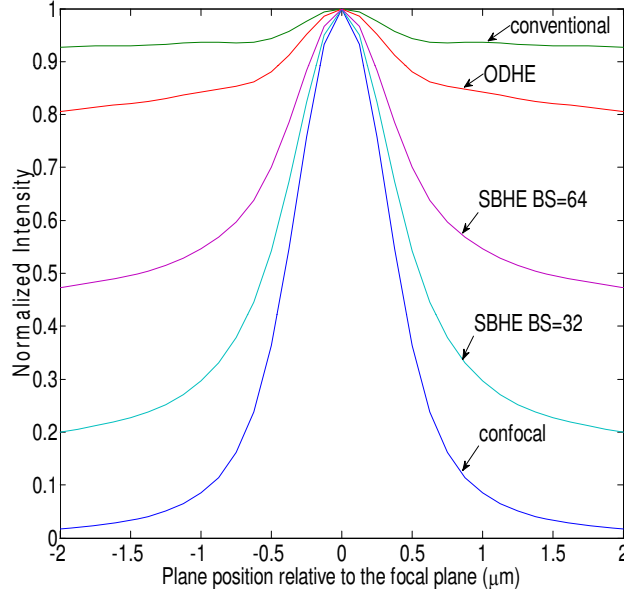


Figure 3. The conjugate measurement of an infinitely thin plane as a function of its relative position to the in-focus plane obtained by CCM with several modulation patterns. The system parameters are set as follows: DMD micromirror size $\rho = 13.68\mu\text{m}$, $\text{NA}=1.4$, $M=100$, excitation wavelength=633nm, emission wavelength=665nm, refractive index=1.515.

better optical sectioning ability compared to the ODHE pattern. The improvement in degree of confocality found arises from the sparsity of SBHE pattern. It turns out that there is a tradeoff between light efficiency and optical sectioning ability. By increasing the block size (BS) of the SBHE pattern, light efficiency increases whereas the degree of confocality decreases. The problem of low light efficiency is not a major problem when operating in reflection mode. While in fluorescence mode, the total number of collected photons greatly determined by the light efficiency, this problem becomes crucial for obtaining high-quality images. However, this low light efficiency could be resolved by using strong fluorophores. It is well known that for the Nipkow disk microscope (light efficiency 1%) equipped with strong fluorophores can yield an image as good as that of a confocal laser scanning microscope (CLSM). Thus, we could expect that CCM with SBHE pattern could also achieve comparative performance as CLSM under strong fluorophores conditions.

2.2 Simulations and Experimental Results

In Fig. 4, we evaluate the performance of CCM as the object thickness changes. The performance of the proposed approach is compared to that yielded by conventional wide-field microscopy. Figure 4(b) shows the resultant images from compressive CM with ODHE patterns obtained by subtracting the recovered nonconjugate image from the recovered conjugate image. Figure 4(c) shows images from compressive CM with SBHE patterns reconstructed using conjugate measurement only. These results show that as the object thickness increases, due to poor optical sectioning ability, the quality of the reconstructed images obtained with conventional microscopy and CCM with ODHE starts to degrade, whereas, as shown in Fig. 3, CCM with SBHE yields much better sectioning capability offering thus higher quality image for thick object compared to that of conventional microscopy. Note that the performance of compressive CM with ODHE is competitive compared to that yielded by conventional microscopy. In this simulation, the total variation minimization algorithm is used for CS image reconstruction.¹²

To further evaluate the performance of the proposed CCM in a real scenario, we design a hardware prototype (testbed) that uses low cost and widely available components. In the experimental setup, shown in Fig. 5(b), the objective used has a magnification of 40 and 0.63 NA. A DC regulated quartz halogen lamp is used as illumination source. The source is collimated and projected to a Texas Instruments DMD of up to 1024×768 , $13.68 \times 13.68 \mu\text{m}^2$ mirrors optimized at the visible spectrum. Each measurement matrix $B^{m,n}$ defines the position of the micro-arrays in the DMD. Figure 5(a) depicts the reconstructed images yielded by the l_1 regularized least square algorithm¹³ with the data captured using the experimental setup for two different modulation patterns with

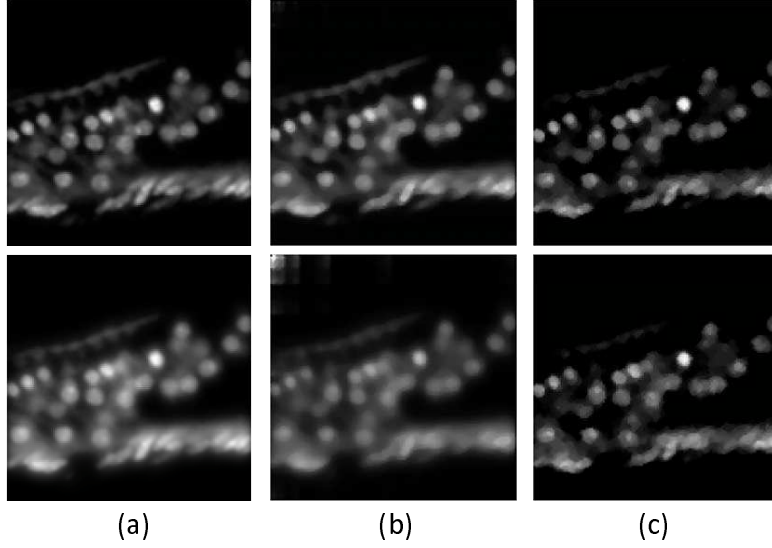


Figure 4. (a) Conventional wide-field imaging. (b) Compressive CM with ODHE pattern. (c) Compressive CM with SBHE pattern, BS=32. Simulation parameters: micromirror size $\rho = 13.68\mu\text{m}$, NA=1.4, refractive index=1.515, excitation wavelength=633nm, emission wavelength=665nm, DMD size 1024×768 , sampling rate=25%, image size= 128×128 . Top: thickness= $0.14\mu\text{m}$. Bottom: thickness $7\mu\text{m}$.

a compression rate of 45%. Note that, the imaging target here is infinitely thin and CCM works in reflection mode. In this case, CCM with ODHE and SBHE patterns yield comparative performance in agreement with the simulation results of an thin object with thickness $0.14\mu\text{m}$.

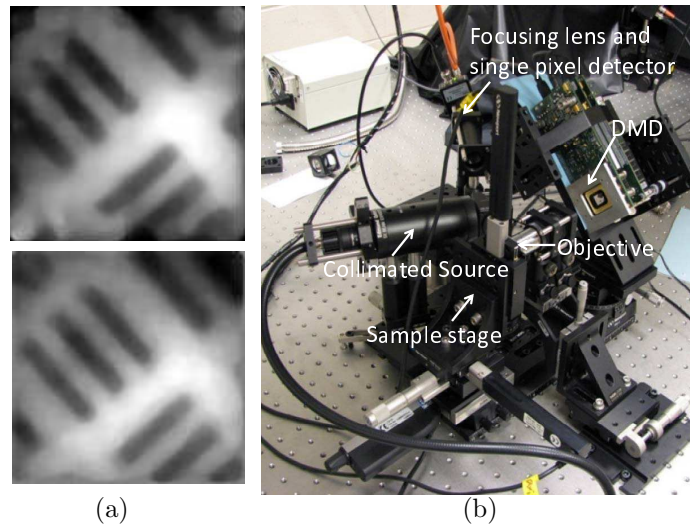


Figure 5. (a) Confocal images reconstructed using measurements obtained from the experimental testbed. Top: ODHE projection patterns and Bottom: SBHE projection patterns, BS=64. For both the sampling rate=45%, image size= 128×128 . Imaging target: USAF-1951, group 5, element 4, 45.25 lp/mm , feature size $11\mu\text{m}$ (b) Experimental setup.

3. THREE-DIMENSIONAL IMAGE RECONSTRUCTION

3.1 Reconstruction Methodologies

In biological applications of confocal microscopy, the overview of an object with axial information is usually required to resolve specific problems. Therefore, it is necessary to study how to realize 3D imaging in compressive

CM. In this section, we propose three methods for 3D image reconstruction. An overview of the three methods is shown in Fig.6

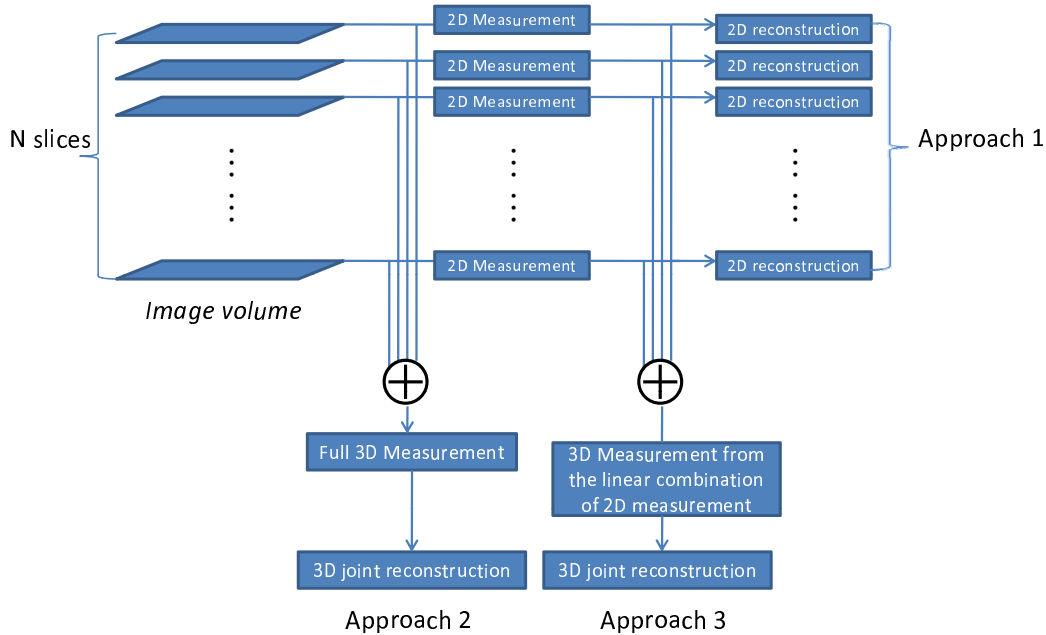


Figure 6. Three-Dimensional image reconstruction algorithms.

Approach 1: 2D slice-by-slice reconstruction

Two-dimensional slice-by-slice reconstruction is achieved by moving the target object along the axial direction, obtaining 2D CS measurements of the corresponding slice at the in-focus plane and reconstructing each image slice independently. l_1 regularized least square algorithm⁹ or total variation minimization¹² can be used to recover the image at the in-focus plane from the set of random measurements. Note that this approach does not exploit the inherent correlation that exists between adjacent slices, but it is computationally inexpensive. Furthermore, this algorithm is highly parallelizable.

Approach 2: 3D joint reconstruction from full 3D measurement

Wakin et al.¹⁴ developed two 3D joint reconstruction methods for video streaming acquisition. In the first method, the measured data is the random projections of one frame. While in the second method, the measured data emerges from the entire frame ensemble. Both methods use 3D wavelets as a sparse representation. The sensing matrix they used is a pseudorandom binary matrix. To load pseudorandom binary patterns onto DMD, however, requires high memory resources and is computational complex. In our 3D reconstruction approaches, instead of using pseudorandom binary patterns, we design a 3D sensing system based on SBHE, which enables lower computation cost, faster image reconstruction and comparatively good image quality as that of dense scrambled Fourier ensemble. Furthermore, compared with 2D slice-by-slice reconstruction, joint 3D reconstruction yields better reconstructed image quality. This improvement is mainly attained because a 3D wavelets basis is used as the sparse basis. 3D data cube has a much sparser representation on 3D wavelets basis than on 2D wavelets basis. As has mentioned in Section 2.1, the number of measurements we need to reconstruct an image is proportional to its sparsity. Therefore, with the same number of measurements, a sparser representation usually leads to higher reconstructed image quality.

The 2D slice-by-slice algorithm can be extended to the 3D case immediately by taking the block Hadamard transform operator, W , in Eq. (8) as a 3D block Hadamard operator, leading thus to a 3D Hadamard transform on each $BS \times BS \times BS$ block within the permuted 3D image. To be more precise, consider a 3D image F of size $N \times N \times N$, $F = \{f_i(m, n)\}$, $i = 1, 2, \dots, N$; $n = 1, 2, \dots, N$; $m = 1, 2, \dots, N$, f_i represents a 2D image

of the i -th slice within the 3D data cube. The joint measurement matrix is defined as:

$$\Phi = \begin{bmatrix} W_B & 0 & \dots & 0 \\ 0 & W_B & \dots & 0 \\ \vdots & \vdots & \ddots & \vdots \\ 0 & 0 & \dots & W_B \end{bmatrix} \times P_{N^3} \quad (9)$$

where W_B represents a 3D Hadamard transform operator for a $BS \times BS \times BS$ volume and P_{N^3} is a pixel-by-pixel 3D permutation operator. The corresponding DMD pattern $B^{m,n,k} = P_{N^3}^{-1} \Phi^{-1} Z^{m,n,k}$, where $Z^{m,n,k}$ is a 3D matrix with only one non-zero entry at the position (m, n, k) . Since DMD is comprised by a 2D mirror array, we need to scan along the z -direction all the N slices in the DMD pattern $B^{m,n,k}$ to obtain one full 3D measurement. Although this method provides better reconstructed image quality than approach 1, the required image acquisition time is N times the acquisition time needed for 2D slice-by-slice reconstruction method. It is even more time-consuming than conventional CM. To overcome this limitation, an alternative 3D reconstruction approach based on 2D measurement is proposed next.

Approach 3: 3D joint reconstruction from 2D measurement

In approach 2, we measure the Hadamard coefficients of a permuted 3D image $F_p = P_{N^3} F$. Now, we relax the requirement for the permutation operator. Instead of performing pixel-by-pixel permutation, we only permute the pixel within each slice. Define such operator as $P_s = \{P_{N^2}^i\}$, $i = 1, 2, \dots, N$, with $P_{N^2}^i$ representing the pixel-by-pixel permutation for the i -th slice. Then the joint measurement matrix is defined as:

$$\Phi = \begin{bmatrix} W_B & 0 & \dots & 0 \\ 0 & W_B & \dots & 0 \\ \vdots & \vdots & \ddots & \vdots \\ 0 & 0 & \dots & W_B \end{bmatrix} \times P_s \quad (10)$$

It will be shown shortly that, the projections of a 3D image onto this joint measurement matrix could be obtained from a linear combination of 2D SBHE measurements of each single slice. For each slice, its 2D SBHE measurements are obtained with the DMD pattern defined in Eq. (8) using $P_{N^2}^i$ as the permutation operator for the i -th slice. Then, the 3D measurements is obtained as follows.

A 3D Hadamard transform of a 3D data cube $F(x, y, z)$ is defined as:

$$H(u, v, w) = \frac{1}{N} \sum_{z=0}^{N-1} \sum_{x=0}^{N-1} \sum_{y=0}^{N-1} F(x, y, z) \mathcal{H}(x, y, z, u, v, w) \quad (11)$$

where $\mathcal{H}(x, y, z, u, v, w)$ represents the transform kernel. Since Hadamard transforms are separable unitary transform, \mathcal{H} can be written as $\mathcal{H}(x, y, z, u, v, w) = h(x, u)h(y, v)h(z, w)$, which means that Eq. (11) can be performed by first transforming each slice of F and then transforming each resultant array along the axial direction to obtain H . Formally,

$$H(u, v, w) = \frac{1}{N} \sum_{z=0}^{N-1} \sum_{x=0}^{N-1} \sum_{y=0}^{N-1} F(x, y, z) h(x, u) h(y, v) h(z, w) = \sum_{z=0}^{N-1} F_{2D}(u, v, z) h(z, w), \quad (12)$$

where h represents an $N \times N$ binary Hadamard matrix, $F_{2D}(u, v, z)$ represents the 2D Hadamard transform of the z -th slice. From Eq. (12), it can be seen that the 3D Hadamard coefficients $H(u, v, w)$ are just the linear combinations of 2D Hadamard coefficients $F_{2D}(u, v, z)$ of different slices in this transformed image. To obtain the 3D Hadamard domain measurements $H(u, v, w)$, we just need to know the 2D Hadamard domain measurements $F_{2D}(u, v, z)$ of all the N slices, $z = 1, 2, \dots, N$, which means that we need to sample at the position (u, v) of Hadamard domain for each slice. So the sampling positions in the 2D Hadamard domain for each slice should be the same. The randomness of the measurement matrix required by CS theory to maintain the incoherence between measurement matrix and sparse basis is conserved by using different permutation operators for different

slices. Using this method, the measurements obtained from each slice could either be used independently for the reconstruction of each slice, or we can use the linear combinations of these measurements to yield the 3D measurements needed for joint 3D reconstruction. The image acquisition time of this method is almost the same as that needed in the 2D slice-by-slice reconstruction method. The time difference mainly lies in the different time required for image reconstruction. The reconstructed image quality with this approach is comparatively good as that yielded by approach 2, but the acquisition time is notably reduced. For both 3D joint reconstruction approaches, l_1 regularized least square algorithm,⁹ total variation minimization¹² and other reconstruction algorithms¹⁵ in CS can be used to recover the 3D data cube.

3.2 Simulations

Figure 7 shows reconstructed images obtained with the three different reconstruction approaches introduced before. In this simulation, we have not considered the optical aspects of the system, but we add some random noise with variance 0.01 to the ideal measurements. l_1 regularized least square algorithm⁹ is used for image reconstruction in the simulations in this section. Figure 8 shows the peak signal to noise ratio (PSNR) for each slice yielded by the various approaches. As is shown in Fig. 8, for different image slices, the reconstructed image quality varies. This difference is partly because the dynamic ranges of the original image slices are different. The average PSNR for all the slices with approach 2 and approach 3 are approximately the same. Compared to the slice-by-slice reconstruction approach, both 3D joint reconstruction methods offer significantly improved image quality. For $128 \times 128 \times 128$ 3D image reconstruction, the average PSNR gain is about 4 dB.

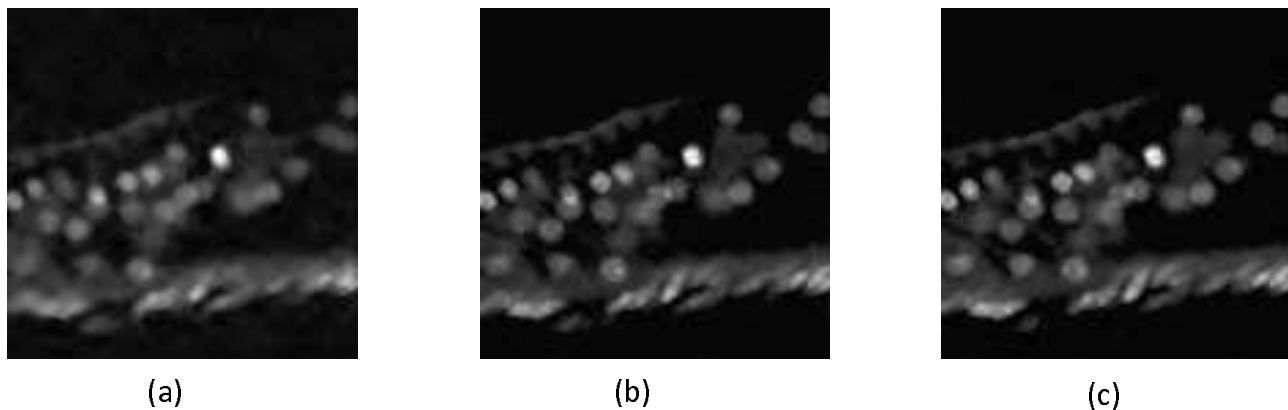


Figure 7. Reconstructed image from SBHE based algorithm, sampling rate=30%, image size= $128 \times 128 \times 128$, reconstruction algorithm: l_1 regularized least square algorithm, additive noise variance=0.01. (a) 2D slice-by-slice reconstruction, PSNR=23.8 dB. (b) 3D joint reconstruction from full 3D measurement, PSNR=29.0 dB. (c) 3D joint reconstruction from 2D measurement, PSNR=28.3 dB.

Now we consider a more realistic scenario where a non-ideal PSF is included in the simulation. The objective used in this simulation has a magnification (M) of 100, 1.4 NA and a refraction index (n) of 1.515. The excitation light wavelength λ_{ex} is 633nm and the emission light wavelength λ_{em} is 665nm. The lateral resolution on the image of the objective $\Delta a = 24.2\mu m$, which is calculated by $\Delta a = 0.51 \frac{\lambda_{em}}{NA} \times M$.¹⁶ Since a single DMD mirror has a pitch of $13.68\mu m < \Delta a$, we use 2×2 DMD pixels to form a square superpixel. Thus for the imaging of a $128 \times 128 \times 128$ 3D volume, the pixel spacing on the object plane should be $273.6nm$. In this simulation, 3D PSF is approximated by a series of 2D PSF on the planes perpendicular to the optical axis, which cover about $3\mu m$ along the axial direction. This is generated by ImageJ Plug-in Diffraction PSF 3D.¹⁷ Figure 9 shows simulation result with the above configuration using method 3.

In this section, we did not discuss ODHE based 3D reconstruction algorithm, because as has been shown in Section 2, CCM with ODHE pattern does not provide good optical sectioning ability. While ODHE based sampling is not well suited for confocal imaging systems, it may provide advantages over SBHE sampling methods in other applications such as video processing, as ODHE sampling patterns exploit “*a priori*” image information.

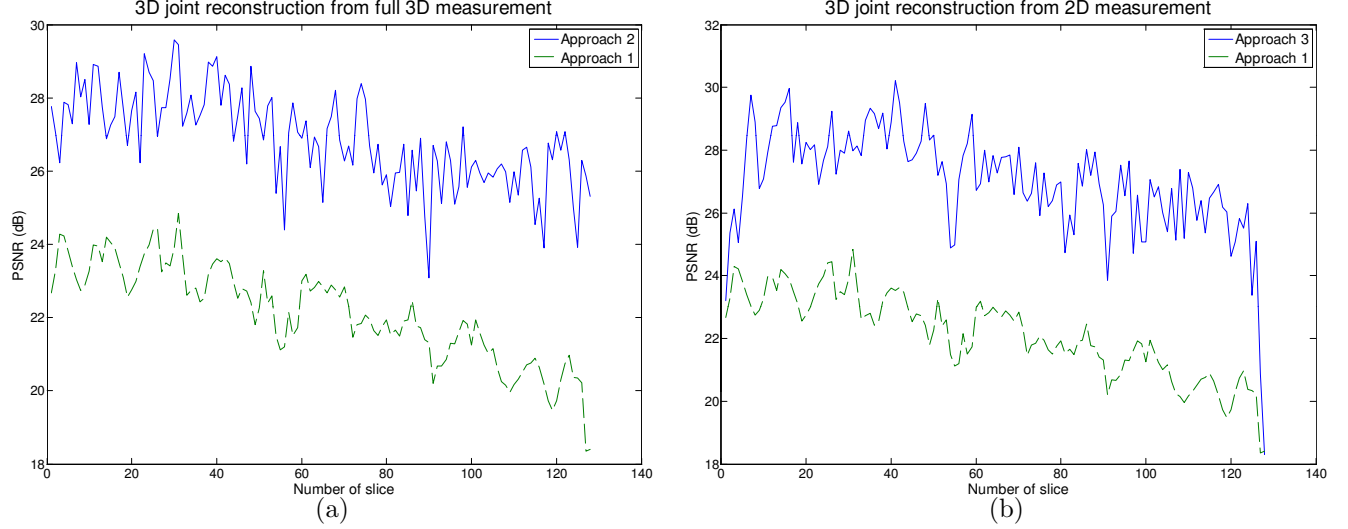


Figure 8. PSNR for $128 \times 128 \times 128$ 3D image, sampling rate 30%. (a) 3D joint reconstruction from full 3D measurement, mean(PSNR)=26.9 dB (b) 3D joint reconstruction from 2D measurement, mean(PSNR)=26.8 dB

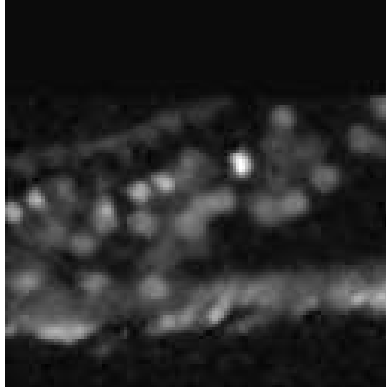


Figure 9. Reconstructed image from SBHE based method 3, sampling rate=30%, image size= $128 \times 128 \times 128$, reconstruction algorithm: l_1 regularized least square algorithm.

4. THEORETICAL ANALYSIS

The performance of the proposed imaging system depends on several factors. The resultant imaging quality can be determined by considering the signal-to-noise ratio (SNR) as the performance measurement of the acquisition system. There are a variety of noise sources in the signal chain. In fluorescence microscopy, where photobleaching limits the total exposure and hence the number of photons that can be detected, photon counting noise (shot noise) would be the dominant component. As it was shown in Ref[18], the number of photons hitting the detector over a time period follows a Poisson distribution with mean equals to its variance. Thus the noise $N = \sqrt{S + B}$, where S and B are, respectively, the number of detected signal and background photons. Then the signal-to-noise ratio $SNR = S/N = S/\sqrt{S + B}$.¹⁸ In CCM, the detected signal contains contributions from all micromirrors at the 'on' position. Thus, if there are K such 'on' positions, and suppose the signal and noise level at each position are the same, then we have $SNR = KS/\sqrt{KS + KB} = \sqrt{KS}/\sqrt{S + B}$. Therefore, compared to conventional imaging system using CCD detectors, CCM offers greatly improved SNR .

In Table 1, we provide a complexity comparison of conventional confocal microscope, compressive confocal microscope (CCM) and programmable array microscope (PAM) with respect to their acquisition time, number of measurement and dynamic range required by the sensor. As for CCM, we consider the configuration required for Approach 1 and Approach 3 that were introduced in Section 3. Assuming that the time (t) to get one snapshot of the image is the same for the three systems. In conventional CM, only one point is measured at a time, therefore

Table 1. Complexity comparison of the three confocal imaging systems.

	Conventional CM	CCM	PAM
Acquisition time	N^3t	$M \times t + t_r$	$(\frac{N^2}{n_x n_y}) \times Nt$
Number of measurement	N^3	M	N^3
Dynamic Range	D	$D \times K$	D

to form the whole $N \times N \times N$ thick image, it requires an acquisition time of N^3t . While in PAM with a grid pattern, if $n_x n_y$ multiple points are measured at one time, the acquisition time will be reduced to $(\frac{N^2}{n_x n_y}) \times Nt$. In CCM, the image formation time that includes the image acquisition time for obtaining the M measurements, $M \times t$, and the time t_r for computing the non-linear optimization program to reconstruct the original image is $Mt + t_r$. Since in CCM, a single detector is used to detect contributions from K illuminated pixels, the dynamic range required is increased from D to KD .

5. CONCLUSIONS

In the proposed CCM, a DMD is used to efficiently scan the 2D or 3D specimen. The measured data in the CCM system emerge from random sets of pinhole illuminated pixels in the specimen that are linearly combined (projected) and measured by a single photon detector. Compared to conventional CM or PAM, the proposed CCM has the potential advantage of simplifying the hardware and optical complexity of confocal imaging systems by off-loading the processing from the data acquisition stage into that of image reconstruction which is software driven leading thus to a lower-cost imaging system. Furthermore, it offers the unique optical sectioning property of confocal imaging at reduced sampling rate. To further improve the system, we designed a 3D joint reconstruction method to fully exploit the correlation between image slices within the 3D image volume. Compared to 2D slice-by-slice method, this method offers significant increased PSNR in reconstructed image, while the computational complexity remains practically the same.

REFERENCES

- [1] Wilson, T., [*Confocal Microscopy*], Academic Press (1990).
- [2] Petran, M., Hadravsky, M., Egger, M. D., and Galambos, R. J., "Tandem-scanning reflected-light microscope," *J. Microsc* **58**, 661–664 (1968).
- [3] Liang, M., Stehr, R. L., and Krause, A. W., "Confocal pattern period in multiple-aperture confocal imaging systems with coherent illumination," *Optics Letters* **22** (June 1 1997).
- [4] Verveer, P. J., Hanley, Q. S., Verbeek, P. W., van Vliet, L. J., and Jovin, T. M., "Theory of confocal fluorescence imaging in the programmable array microscope (PAM)," *J. Opt. Soc. Am.* **3**, 192–198 (1998).
- [5] Wilson, T., Juskaitis, R., Neil, M. A. A., and Kozubek, M., "Confocal microscopy by aperture correlation," *Optics Letters* **21** (December 1996).
- [6] Candés, E., Romberg, J., and Tao, T., "Robust uncertainty principles: Exact signal reconstruction from highly incomplete frequency information," *IEEE Trans. Information Theory* **52**, 489–509 (2006).
- [7] Candés, E. and Tao, T., "Near-optimal signal recovery from random projections and universal encoding strategies?," *IEEE Trans. Information Theory* **52**, 5406–5245 (2006).
- [8] Ye, P., Paredes, J. L., Arce, G. R., Wu, Y., Chen, C., and Prather, D. W., "Compressive confocal microscopy," *Proc. ICASSP* (April. 2009).
- [9] Kim, S.-J., Koh, K., Lustig, M., Boyd, S., and Gorinevsky, D., "An interior-point method for large-scale l_1 -regularized least squares," *IEEE Journal of selected topics in Signal Processing* **1** (Dec. 2007).
- [10] Gan, L., Do, T. T., and Tran, T. D., "Fast compressive imaging using scrambled block hadamard ensemble," (2008). Preprint.
- [11] Do, T. T., Tran, T. D., and Gan, L., "Fast compressive sampling with structurally random matrices," *Proc. ICASSP* (Mar. 2007).
- [12] Candés, E. and Romberg, J., "L1magic: Recovery of sparse signals via convex programming." Caltech (Oct. 2005).

- [13] Koh, K., Kim, S., and Boyd, S., "l1_ls : A matlab solver for large-scale l1-regularized least squares problems." Stanford University (Mar. 2007).
- [14] Wakin, M., Laska, J., Duarte, M., Baron, D., Sarvotham, S., Takhar, D., Kelly, K., and Baraniuk, R., "Compressive imaging for video representation and coding," *Picture Coding Symposium - PCS 2006* (April 2006).
- [15] Candés, E. and Romberg, J., "Practical signal recovery from random projections," *SPIE International Symposium on Electronic Imaging: Computational Imaging III* (January 2005). San Jose, California.
- [16] Wilhelm, S., Grobler, B., Gluch, M., and Heinz, H., "Confocal laser scanning microscopy," available online: [http://www.zeiss.com/c1256d18002cc306/0/f99a7f3e8944eee3c1256e5c0045f68b/\\$file/45-0029_e.pdf](http://www.zeiss.com/c1256d18002cc306/0/f99a7f3e8944eee3c1256e5c0045f68b/$file/45-0029_e.pdf).
- [17] Dougherty, B., "Diffraction psf 3d," (2005). Online, <http://www.optinav.com/Diffraction-PSF-3D.htm>.
- [18] Sandison, D. R. and Webb, W. W., "Background rejection and signal-to-noise optimization in confocal and alternative fluorescence microscopes," *Applied Optics* **33**, 603-615 (1994).